JOURNAL OF SYNCHROTRON RADIATION

ISSN 1600-5775

Generation of apodized X-ray illumination and its application to scanning and diffraction microscopy

Krishna P. Khakurel,[a,b] Takashi Kimura,[a,b] Hiroki Nakamori,[c,d] Takumi Goto,[d] Satoshi Matsuyama,[d] Tomoya Sasaki,[a,b] Masashi Takei,[a] Yoshiki Kohmura,[e] Tetsuya Ishikawa,[e] Kazuto Yamauchi[d] and Yoshinori Nishino[a,b]*

[a]Research Institute for Electronic Science, Hokkaido University, Kita 21, Nishi 10, Kita-ku, Sapporo 001-0021, Japan, [b]Graduate School of Information Science, Hokkaido University, Kita 21, Nishi 10, Kita-ku, Sapporo 001-0021, Japan, [c]JTEC Corporation, Saito-Yamabuki, Ibaraki, Osaka 567-0086, Japan, [d]Department of Precision Science and Technology, Graduate School of Engineering, Osaka University, 2-1 Yamadaoka, Suita, Osaka 565-0871, Japan, and [e]SPring-8/RIKEN, 1-1-1 Kouto, Sayo-cho, Sayo-gun, Hyogo 679-5148, Japan.
*Correspondence e-mail: yoshinori.nishino@es.hokudai.ac.jp

Received 7 May 2016
Accepted 5 November 2016

Edited by Y. Amemiya, University of Tokyo, Japan

Keywords: X-ray deformable mirrors; apodized X-ray illumination; hard X-ray microscopy.

X-ray science has greatly benefited from the progress in X-ray optics. Advances in the design and the manufacturing techniques of X-ray optics are key to the success of various microscopic and spectroscopic techniques practiced today. Here the generation of apodized X-ray illumination using a two-stage deformable Kirkpatrick–Baez mirror system is presented. Such apodized illumination is marked by the suppression of the side-lobe intensities of the focused beam. Thus generated apodized illumination was employed to improve the image quality in scanning X-ray fluorescence microscopy. Imaging of a non-isolated object by coherent X-ray diffractive imaging with apodized illumination in a non-scanning mode is also presented.

1. Introduction

Nano-scale X-ray imaging has undergone an enormous development largely due to the progress made in X-ray focusing optics as well as light sources (Sakdinawat & Attwood, 2010; Ice *et al.*, 2011). The utilization of focused X-ray illumination in various forms of X-ray microscopic techniques, such as scanning X-ray fluorescence microscopy (SXFM) (Fahrni, 2007; De Jonge & Vogt, 2010; Fittschen & Falkenberg, 2011; Majumdar *et al.*, 2012; Matsuyama *et al.*, 2010) and coherent diffractive imaging (CDI) (Miao *et al.*, 1999, 2015; Robinson & Harder, 2009), has become routine and has served to improve the performance of these techniques (Schroer *et al.*, 2008; Takahashi *et al.*, 2009). The focused beam profile is usually accompanied by the side-lobes in addition to the main lobe, and the spatially extended nature of focused illumination due to the side-lobes either decline or limit their performances. For instance, the presence of the side-lobes in the focused illumination declines the practically obtainable resolution of the images in SXFM. Also, in the realisation of CDI of extended objects, both in the scanning and non-scanning mode, localized illumination is indispensable. For the extension of the applications of these techniques, elimination or substantial suppression of side-lobe intensities in the focused illumination is a must. Recently, the authors have proposed an optical design to generate spatially localized focused illumination, where side-lobe intensities are largely suppressed, and have presented a numerical simulation on the use of such apodized illumination in imaging non-isolated objects by non-scanning CDI (Kimura *et al.*, 2013). In

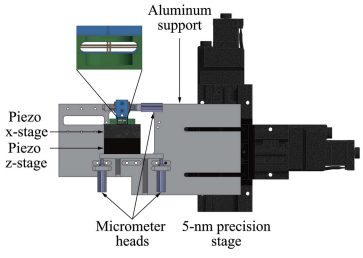

this article, we present the realisation of such an optical setup employing a two-stage deformable Kirkpatrick–Baez (KB) mirror system to generate the apodized illumination. As proof-of-principle experiments, we also demonstrate the enhancement of the resolution in SXFM and the imaging of an extended test object by apodized-illumination CDI.

In scanning microscopy, such as SXFM, the probe size limits the resolution. The adverse effect of the extended spatial illumination on scanning microscopy and the benefit of the apodized illumination to improve the image quality has been widely discussed in visible-light microscopy (Webb, 1996; Gauderon *et al.*, 1999). Though the image formation mechanism in SXFM differs from that of its optical counterpart, the amelioration of the image quality by apodized illumination is expected.

CDI is a lensless imaging technique, in which the image formation is computationally performed from the coherent diffraction pattern by employing phase retrieval algorithms (Fienup, 1982). Practically, only isolated samples can be measured owing to the necessity of the satisfaction of the oversampling condition (Miao *et al.*, 1998). Ptychography, a scanning diffractive imaging method, routinely performs the imaging of extended objects across various wavelengths (Rodenburg *et al.*, 2007; Thibault *et al.*, 2008; Maiden *et al.*, 2010; Marrison *et al.*, 2013; Thibault & Menzel, 2013; Shapiro *et al.*, 2014). However, a non-scanning method is preferred to capture fast dynamics. In addition, scanning methods also fall short in imaging extended objects with intense ultra-short pulses from X-ray free-electron lasers (XFELs), where the sample is destroyed immediately after the scattered pulse leaves the sample. Apodized-illumination CDI can potentially overcome these challenges and image the extended object with the focused illumination avoiding the necessity of multiple recording of coherent diffraction patterns. Apodized-illumination CDI of extended objects has recently been demonstrated with visible light (Khakurel *et al.*, 2015). Here we present an approach to extend the method to X-ray wavelengths.

2. Experimental setup

We performed an experiment to generate a focused illumination with suppressed side-lobe intensities at the experimental hutch 3 (EH3) of BL29XU, an undulator beamline with an overall length of 1 km, at SPring-8 (Tamasaku *et al.*, 2001). A schematic of the optical system is shown in Fig. 1. The optical system comprises two pairs of deformable mirrors (Kimura *et al.*, 2009), each aligned in the KB geometry (Kirkpatrick & Baez, 1948). All of the mirrors were fabricated in an ultra-precise manner such that the wavefront distortion by the surface roughness is smaller than that required by the Rayleigh criterion for ideal focusing. For the mirrors used in the system, the Rayleigh criterion requires the surface roughness to be less than 4 nm while the measured value is ∼2 nm (Matsuyama *et al.*, 2016). It is known that a single elliptical KB mirror system causes comatic aberration. In our optical system, two sets of KB mirror systems are placed in the (+, +) configuration [both vertical and horizontal mirrors are in the (+, +) configuration] for easier handling. In this case, geometrical optics considerations show that the amount of comatic aberration increases additively. However, when using two sets of KB mirror systems in the (+, −) configuration, the Abbe sine condition is satisfied and the comatic aberration can be removed. A detailed explanation of the alignment and deformation process of the two-stage deformable KB mirror system is discussed elsewhere (Matsuyama *et al.*, 2016).

A slit in the transport channel of the beamline, the TC1 slit, defines the beam shape and size. The beam defined by the TC1 slit behaves as the virtual source for the constructed optical system. The coherence area at the entrance of the two-stage deformable KB mirror system, which is located ∼50 m downstream of the TC1 slit, can be adjusted by varying the aperture size of the TC1 slit. For diffraction-limited focusing, the coherence area larger than the entrance aperture of a focusing optics is required. A numerical-aperture-defining slit was installed just before the two-stage deformable KB mirror system to regulate the entrance aperture. An ionization chamber immediately behind the numerical-aperture-defining slit provides the incident photon flux.

The deformable KB mirror system closer to the TC1 slit will be referred to as the upstream mirror system and the farther one as the downstream mirror system. The upstream mirror system with a one-dimensional elliptical shape is designed such that its front focus is at the TC1 slit. At the back focal plane of the upstream mirror system, we placed an apodizing slit. The apodizing slit functions to remove the side-lobe

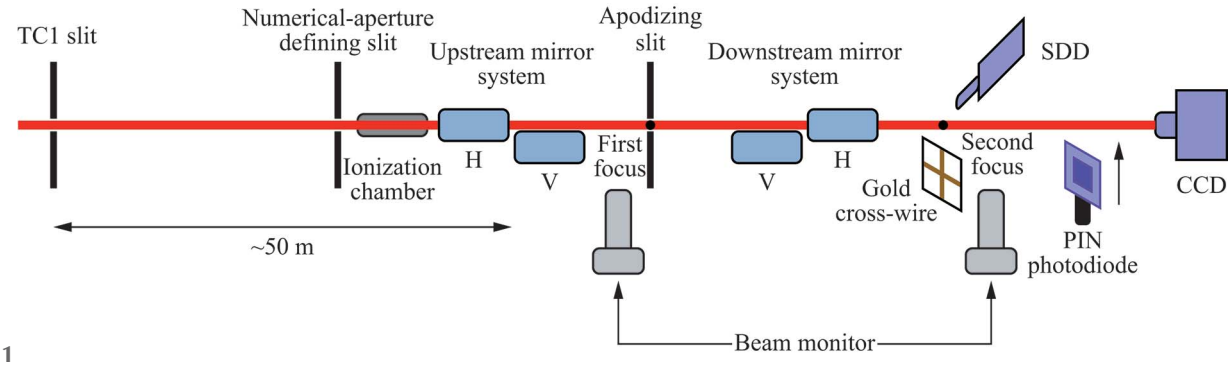

Figure 1
Schematic of the experimental setup.

Table 1
Optical parameters of the mirrors.

		SXFM measurement		CDI measurement	
	Glancing angle	Front focal length	Back focal length	Front focal length	Back focal length
Upstream mirror system (horizontal)	4 mrad	∼50 m	1250 mm	∼50 m	750 mm
Upstream mirror system (vertical)	4 mrad	∼50 m	1120 mm	∼50 m	620 mm
Downstream mirror system (horizontal)	4 mrad	250 mm	300 mm	750 mm	300 mm
Downstream mirror system (vertical)	4 mrad	120 mm	430 mm	620 mm	430 mm

intensities of the beam focused with the upstream mirror system. A detailed discussion on the design, construction and the alignment procedure of the apodizing slit will be presented later in this article.

The front focus of the downstream mirror system was designed to coincide with the back focal plane of the upstream mirror system, and the common focus is hereafter called the first focus. The image of the beam profile in the first focal plane is then formed at the back focal plane of the downstream mirror system, the second focal plane. The side-lobe intensities at the second focus can be suppressed by optimizing the aperture size and position of the apodizing slit. The illumination with suppressed side-lobe intensities at the second focus will be hereinafter termed as apodized illumination. At the second focal plane, we installed xz translation stages with a positional precision of 1 nm (the 1 nm-precision stages), on which the samples and the gold cross-wire of 200 µm diameter for focused-beam profile measurement are mounted.

The optical system realises variable focal spot size at the fixed sample position by changing the first focal position with the deformable mirrors. We set a limit on the range of the first focal position so that the convergence angle of the upstream mirror does not exceed the angular acceptance of the downstream mirror. The convergence angle of the upstream mirror and the angular acceptance of the downstream mirror are given by a_u/f_{ub} and a_d/f_{df}, respectively. Here, f_{ub} is the back focal length of the upstream mirror, and f_{df} is the front focal length of the downstream mirror. a_u and a_d are the aperture sizes of the upstream and downstream mirrors, respectively, and are expressed as $a_u \simeq l_u\theta_u r_a$ and $a_d \simeq l_d\theta_d$, where l_u and l_d are the lengths and θ_u and θ_d are the glancing angles of the upstream and downstream mirrors, respectively. r_a is the aperture ratio set by the numerical-aperture-defining slit. Since the length and the glancing angle are the same for all four mirrors in our system, $l_u = l_d = 100$ mm and $\theta_u = \theta_d = 4$ mrad, the optical system was so designed to keep f_{df} equal to or shorter than f_{ub}. Different focal spot sizes at the sample position were used for the SXFM and CDI experiments. The parameters of the mirror systems for both cases are summarized in Table 1.

The optical system also contains retractable beam monitors at the first and second focuses used in the alignment and deformation of the mirrors. These beam monitors also facilitate the alignment of the apodizing slit and coarse determination of the sample positions. An escapable PIN photodiode is placed 0.4 m downstream of the sample plane and is used to measure the beam profiles at the back focal planes of both the mirror systems by the knife-edge scan. A silicon drift detector (SDD), for the detection of fluorescent X-rays, was placed off-axis and physically close (∼15 mm) to the sample. In the CDI mode, a charge-coupled device (CCD) is placed at 2.51 m downstream of the sample plane in the Fraunhofer regime to satisfy the oversampling condition and is used to record the coherent X-ray diffraction (CXD) patterns. A beam-stop is placed immediately in front of the detector to prevent the detector from potential damage due to the intense direct X-ray beam reflected from the optical system. The path in between the sample and the detector was evacuated to a pressure of the order of 10^{-3} Pa. The PIN photodiode and the SDD were moved out of the X-ray path during the CDI measurement.

3. Design of the apodizing slit system and the apodization experiment

In designing the apodizing slit, a precision substantially smaller than the focused beam size is required. Additionally, all the blades of the apodizing slit need to be within the depth of focus of the upstream mirror system and the depth of field of the downstream mirror system. The depth of focus of the upstream mirror is given by $\sim \lambda/(2\mathrm{NA}_u^2)$, where λ is the wavelength and NA_u is the numerical aperture of the upstream mirror. As for the depth of field of the downstream mirror, a straightforward calculation in geometrical optics gives $\sim (f_{df}^2 x)/(\mathrm{NA}_d f_{db}^2)$. Here, f_{df} and f_{db} represent the front and back focal lengths of the downstream mirror, respectively. NA_d is the numerical aperture of the downstream mirror and x is the size of the circle of confusion. When using the spot size $\sim\lambda/(2\mathrm{NA}_d)$ of the second focus as x, we obtain $(\lambda f_{df}^2)/(2\mathrm{NA}_d^2 f_{db}^2)$ as the depth of field of the downstream mirror. The smallest depth of focus of the upstream mirror and the smallest depth of field of the downstream mirror are obtained when the first focus is at the middle of the two KB mirror systems (the first focus is farthest from the downstream mirror system) as in our CDI experiment described below. In this case, the mathematical expressions of the depth of focus of the upstream mirror and the depth of field of the downstream mirror coincide. The smallest depth in our experiment (the CDI experiment) is given by 1.84 mm.

Fig. 2 shows a drawing of the entire structure of the apodizing slit system we designed. The apodizing slit rests on the aluminium support, which is mounted on a two-axis translation stages with a positional precision of 5 nm. Four gold wires with a diameter of 200 µm are used as the blades of the apodizing slit and are installed as two pairs of a perpendicular cross-wire to define the rectangular aperture. One of

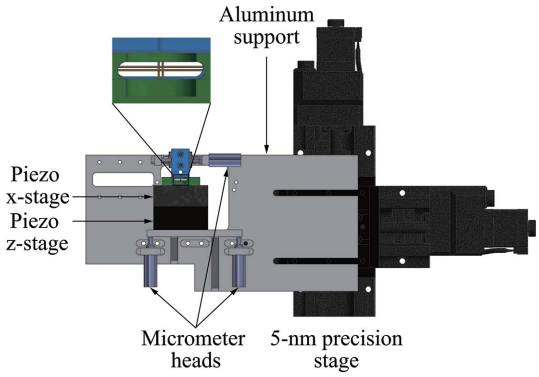

Figure 2
Drawing of the apodizing slit system. The zoomed image shows the arrangement of the four gold wires used as the slit blades.

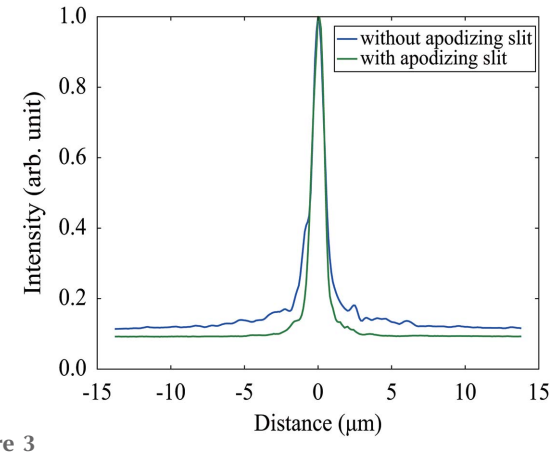

Figure 3
Comparison of the experimental profiles at the back-focal plane of the downstream mirror system with and without the apodizing slit.

the cross-wires is fixed to the aluminium support. The aperture size can be changed by translating the other pair of cross-wires attached to *xz* piezo stages (Physik Instrumente), which is connected to the aluminium support through a flexure hinge. The travel range of both the piezo stages is 100 μm. There are also three micrometer-heads for coarse adjustment of the slit aperture and the parallelism of the two cross-wires.

The aperture size of the apodizing slit was optimized in two steps. In the first step, the aperture size was coarse-tuned by using the micrometer heads before installing the apodizing slit system in EH3. The coarse tuning involved the reduction of the aperture size to less than 100 μm × 100 μm, a constraint set by the travel range of the *xz* piezo stages used. In addition, the parallelism of the two cross-wires was optimized with a precision of better than 2 mrad by using two micrometer-heads beneath the *xz* piezo stage. All four gold wires were placed within 800 μm along the X-ray path as confirmed by using the beam monitor at the first focus, which is smaller than the depth of focus of the upstream mirror system and the depth of field of the downstream mirror system.

In the second step, the aperture size and the position of the apodizing slit were adjusted on-line using the piezo stages by measuring the beam profile at the first and the second focuses. The beam profiles at the first and the second focuses were measured by employing the bright-field and dark-field knife-edge scanning method (Suzuki *et al.*, 2005), respectively, using the PIN photodiode. Determination of the rough positions of the apodizing slit was carried out by observing the first minimum in the illumination profiles measured at the first focus. The apodizing slit size was then optimized by observing the dark-field knife-edge scanning profiles measured at the second focus.

For apodization and SXFM experiments, X-rays with a photon energy of 10 keV and a virtual source (TC1 slit) size of 10 μm × 10 μm were used. The measured focal spot sizes (full width at half-maximum) at the back focal plane of the upstream and downstream mirror system were 650 nm × 1500 nm and 1000 nm × 1800 nm, respectively. The aperture size and position of the apodizing slits were optimized with an accuracy of ±200 nm. A comparison of the horizontal intensity profile at the second focus with and without the apodizing slit is shown in Fig. 3. The profiles were measured by dark-field knife-edge scanning method with a scan step size of 100 nm. It is apparent from the graph that the use of the apodizing slit made the illumination profiles smoother and the side-lobe intensities were suppressed.

4. SXFM with apodized illumination

SXFM provides elemental maps by detecting characteristic fluorescent X-rays at different sample positions. We performed SXFM measurement for a chromium mesh pattern by using the focused apodized illumination.

An optical micrograph of the chromium mesh pattern is shown in Fig. 4(*a*). The mesh pattern is composed of 5 μm half-pitch line and space patterns in both directions and fabricated on a 200 nm-thick silicon nitride (SiN) membrane substrate using electron beam lithography. We employed the lift-off process, which involves spin-coating of the photo-resist (ZEP 520A), electron beam writing (ELIONIX ELS-F125), development, deposition of the chromium, and finally the wet-etching using dimethylacetamide (ZDMAC). The chromium was deposited by a compact sputter system (ULVAC ACS-4000-C3-HS) and the thickness of the deposited layer is ∼5 nm. The patterned area on the SiN membrane was 500 μm × 500 μm.

The fabricated test pattern was mounted on the 1 nm-precision stage in the sample plane. The X-ray fluorescence from the chromium was measured by the SDD (X-Flash Detector type 1201, Röntec Co. Ltd). The sample was scanned with the focused beam with a step size of 200 nm. At each position the sample was exposed for 5 s, which was found to be long enough to collect adequate signals to generate the contrast in the image. The line profiles of Cr *Kα* fluorescence along the horizontal direction of the sample with and without the apodizing slit are shown in Fig. 4(*b*). With the employment of the apodizing slit, the background noise was significantly reduced. This means that the side-lobe intensities caused the enhancement of the background intensity. Also, the image measured with the optimized apodizing slit has slightly sharper edges than the image without the apodizing slit,

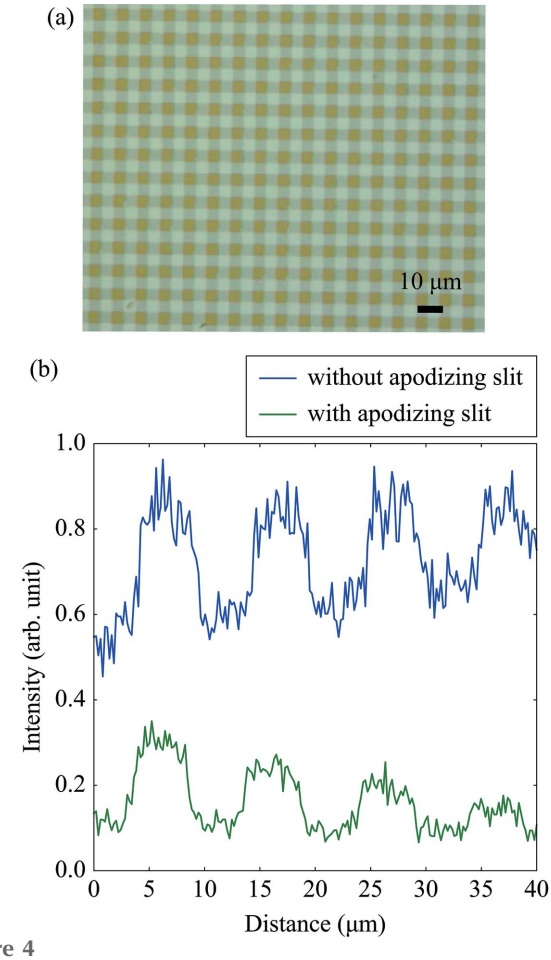

Figure 4
SXFM experiment. (*a*) Optical micrograph of the chromium mesh pattern used as a test object in SXFM measurement. (*b*) One-dimensional map of Cr *Kα* fluorescence of the test object measured by SXFM.

providing an indication of improvement in the resolution of the image with the apodized illumination. Defining the contrast as the ratio of the maximum to the minimum intensities of the line profiles, we obtained contrast values of 5.2 and 2.1 with and without apodization, respectively. Hence, an enhancement of the contrast by a factor of ∼2.5 was achieved by apodization.

We also performed a numerical simulation of SXFM and show the results in Fig. 5. We used the focused beam profiles shown in Figs. 5(*a*) and 5(*b*) with and without apodization, respectively, obtained by wave-optical simulation in our previous work (Kimura *et al.*, 2013) with an appropriate scaling. A binary mesh pattern shown in Fig. 5(*c*) was taken as the sample. It is obvious from the line profiles in Fig. 5(*d*) that apodized illumination helps to suppress the background intensity significantly. This observation is consistent with our experimental result.

5. Coherent diffractive imaging with apodized illumination

We performed a CDI experiment for a 1 μm grid pattern in the NTTAT-test chart (NTT-AT XRESO-50HC) shown in

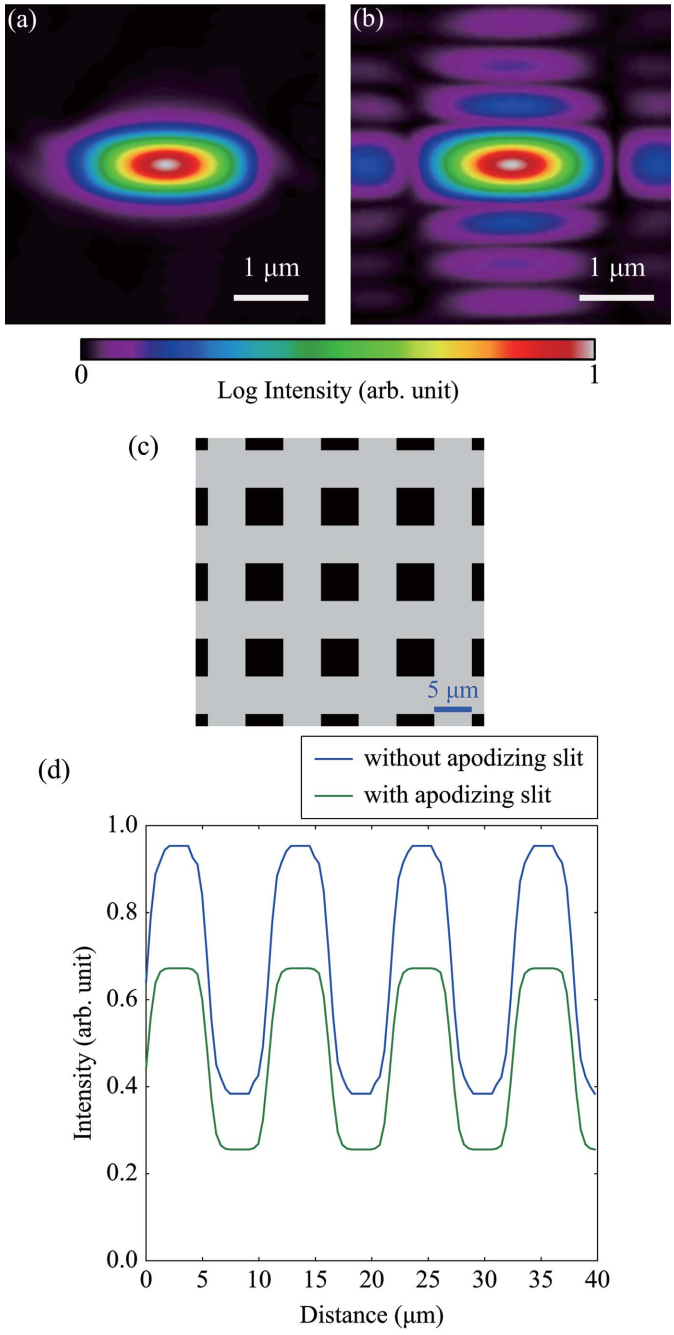

Figure 5
Numerical simulation of SXFM. Illumination at the sample plane obtained by wave-optical simulation (*a*) with and (*b*) without apodizing slit. (*c*) Binary mesh pattern used as a sample. (*d*) Horizontal line profiles of simulated SXFM data obtained using illuminations (*a*) and (*b*).

Fig. 6(*a*). In the grid pattern, the width of each line is 250 nm and the distance between two adjacent lines is 750 nm. The X-ray photon energy was 9 keV, and the virtual source size was 20 μm × 20 μm. The mirror parameters used for the CDI experiment as shown in Table 1 produces the narrowest X-ray beam for the designed optical system. The scattering from the edge of the mirror can deteriorate the quality of the apodized illumination. In order to avoid such circumstances, the numerical-aperture-defining slit was adjusted such that only 60% of the total effective aperture of the mirror is illuminated.

For the optical configuration used for the CDI experiment, the measured spot size (full width at half-maximum) at the first and second focuses are 600 nm × 400 nm and 400 nm × 650 nm, respectively. In the measurement of CXD patterns, a pair of X-ray cross slits was placed immediately before the sample in order to cut off the parasitic scattering from the optical system.

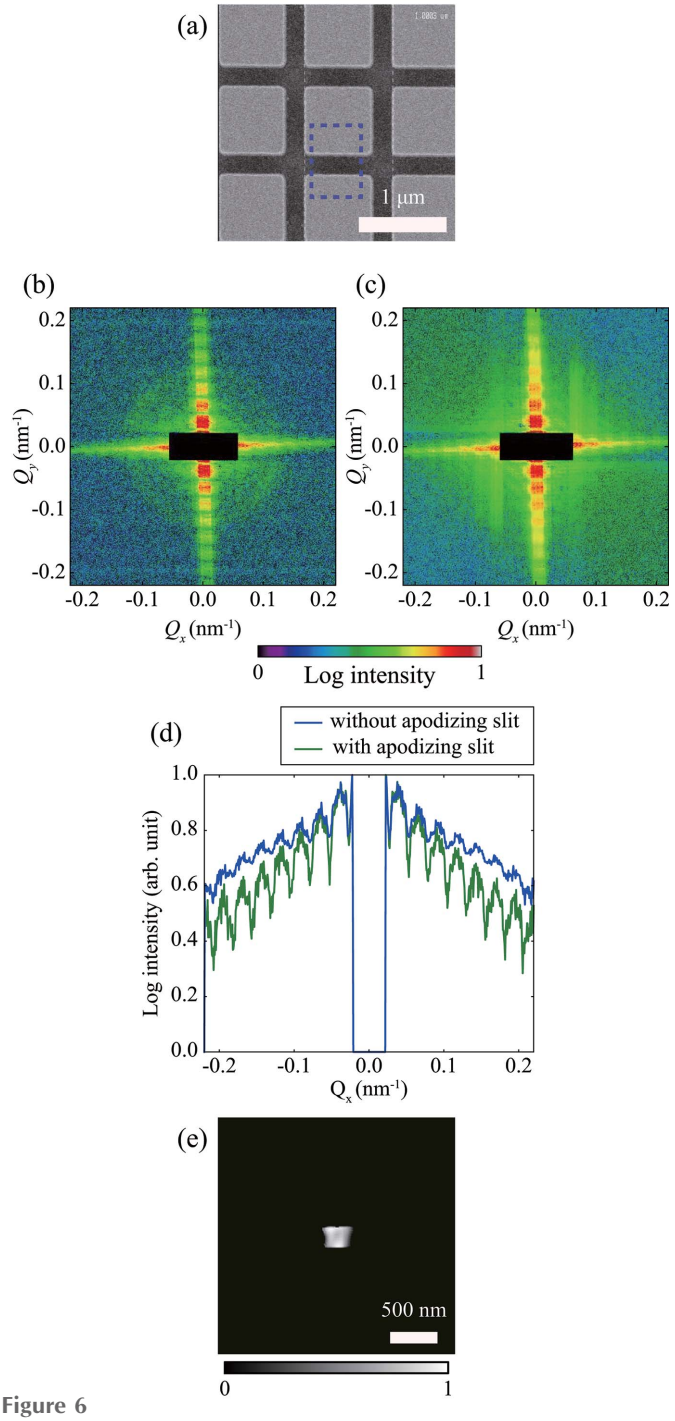

Figure 6
CDI experiment. (*a*) The 1 μm grid pattern in the NTTAT-test chart used as a sample in the CDI experiment. CXD patterns (*b*) with the apodizing slit at the optimized aperture size and position and (*c*) without the apodizing slit. (*d*) Comparison of the visibility of the fringes in the CXD patterns (*b*) and (*c*). The axes Q_x and Q_y in the graphs are defined as $Q_x = (4\pi/\lambda)\sin(\theta_x/2)$ and $Q_y = (4\pi/\lambda)\sin(\theta_y/2)$, respectively. Here, λ is the wavelength and θ_x and θ_y are the scattering angles along the x and y direction, respectively. (*e*) Reconstructed image from the CXD pattern shown in (*b*) with apodizing slit.

CXD patterns were recorded with an X-ray CCD (Princeton Instruments PI-LCX: 1300) consisting of 1340 × 1300 pixels, each of area 20 μm × 20 μm. The CCD, operated in vacuum, was cooled to a temperature of 173 K with liquid nitrogen in order to reduce the dark-current noise. The sample–detector distance (l) in the experimental results presented below was 2.51 m. With this optical configuration the minimum oversampling ratio, given by $\sigma = \lambda l/\delta a$, is ∼13, where λ is the X-ray wavelength, δ is the pixel size and a is the largest dimension of the incident illumination at the sample plane. We used the CXD data in the central 1200 × 1200 pixel of the CCD. The CXD patterns shown in this article are those after subtraction of the background noise and binning by a factor of two in each direction. The pixel size of reconstructed images is ∼14 nm as determined from the experimental geometry.

The CXD patterns with and without the apodizing slit are shown in Figs. 6(*b*) and 6(*c*), respectively. The total exposure time for each CXD pattern was 600 s. The line profile shown in Fig. 6(*d*) is plotted along the vertical fringe in the CXD patterns. The profiles clearly show an improvement in the visibility of the CXD pattern with apodized illumination. In general, CXD patterns contain speckles, and the minimum speckle size for extended objects is inversely proportional to the illumination size. When using apodized confined illumination, the CCD can resolve each speckle. However, for non-apodized extended illumination, the speckle can be too small to be resolved by CCD which can cause deterioration of the visibility of the CXD patterns.

We performed a numerical simulation to verify the effect of apodization on the fringe visibility of CXD patterns. We again used focused beam profiles with and without apodization obtained by wave-optical simulation in our previous work (Kimura *et al.*, 2013) with an appropriate scaling. The grid pattern shown in Fig. 7(*a*) was used as the sample. Figs. 7(*b*) and 7(*c*) show the exit wave with and without apodization. The simulated CXD patterns with and without apodization are shown in Figs. 7(*d*) and 7(*e*), respectively. The line profiles along the vertical fringe of the CXD patterns in Fig. 7(*f*) apparently show that the visibility of the CXD pattern improves significantly with apodized illumination, and supports well our experimental observation.

We used a combination of shrink-wrap hybrid input–output algorithm (HIO) (Marchesini *et al.*, 2003) and error reduction (ER) algorithm for image reconstruction from the CXD pattern. The support size was initially set to be slightly larger than the illumination size. The support was then gradually updated by convoluting the reconstructed image with a Gaussian function. The width of the Gaussian function was initially set to be 2.0 pixels and was reduced by 1% every 50 iterations. The threshold for the dynamic support was set to 8% of the maximum of the reconstruction. The reconstructed image in Fig. 6(*e*) was obtained after a total of 10000 iterations,

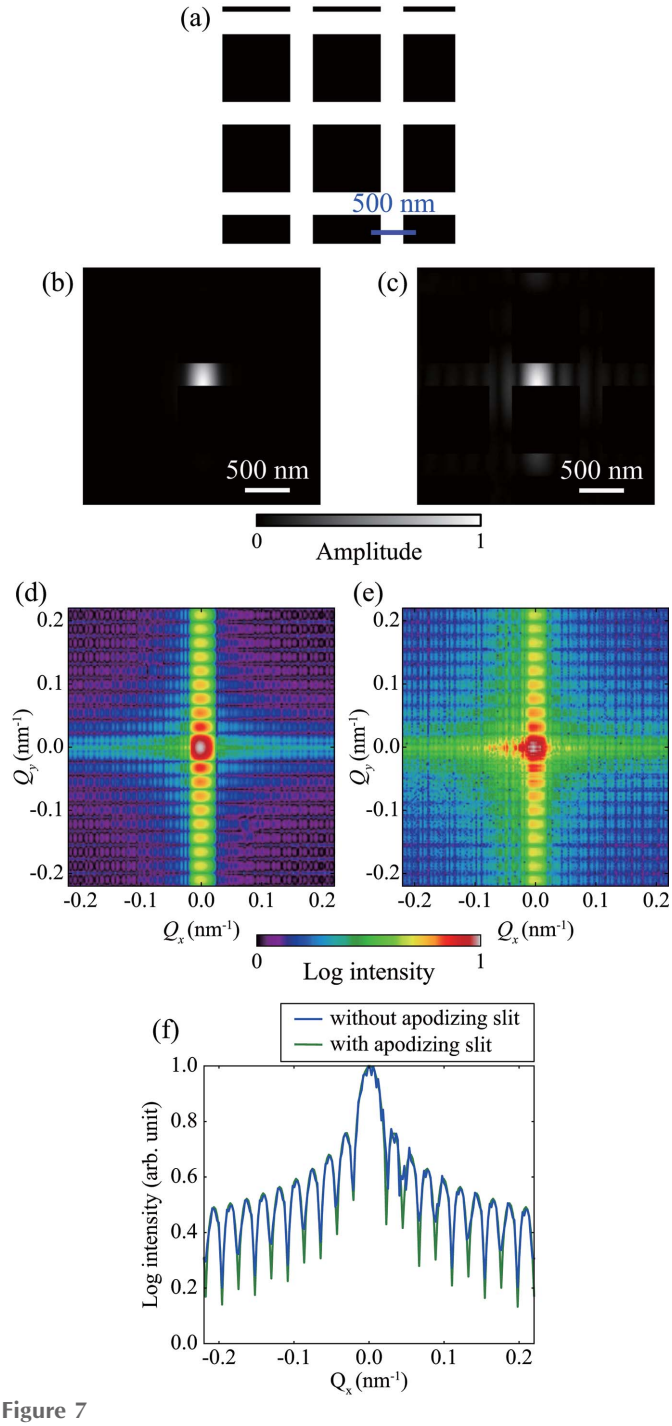

Figure 7
Numerical simulation of CDI. (*a*) Binary mesh pattern used as a sample. Exit wave from the sample using wave-optically simulated illumination (*b*) with and (*c*) without apodizing slit. Simulated diffraction patterns (*d*) obtained from (*b*), and (*e*) obtained from (*c*). (*f*) Line plot along the vertical fringe through the center in the diffraction patterns (*d*) and (*e*).

of which the first 5000 were performed with the shrink-wrap HIO and the last 5000 with the shrink-wrap ER. The line pattern in the reconstructed image is in agreement with the line in the 1 µm grid pattern as shown in Fig. 6(*a*). The dotted line in Fig. 6(*a*) represents the position of the focused illumination. The experimental results of apodized-illumination CDI presented in the present paper and the previous work for visible light (Khakurel *et al.*, 2015) demonstrate that one can obtain images of extended objects of reasonable quality with apodized illumination and conventional phase-retrieval algorithms. For the determination of the true density distribution in the sample, reconstructed images should be normalized by the amplitude of the apodized illumination.

6. Conclusions

In summary, we have constructed a two-stage deformable KB mirror system to generate apodized illumination. The apodized illumination thus generated has a smoother profile compared with the one without the apodizing slit. In the process, we have designed, constructed and tested a compact X-ray cross-slit with precisely controllable aperture size.

SXFM measurement was performed with a test object using the apodized illumination and a distinct indication of improvement in the resolution has been observed. We expect that the effect of apodized illumination on SXFM results will be more pronounced and meritorious when the focal spot size is much smaller than that used in the current experiment. The effect of apodization has also been observed in the CXD patterns of the non-isolated object. An improvement in the visibility of the fringe in the CXD pattern with apodized illumination has been observed. We have also presented the coherent X-ray diffractive imaging of a non-isolated object in a non-scanning mode.

In SXFM and CDI experiments, we realised different focal spot sizes at a fixed sample position by using a two-stage deformable KB mirror system. In this way, a unique feature of the optical system to generate variable focal spot size at a fixed focal point has been demonstrated. We expect that the optical system discussed here will find wide applications in various spectroscopic and microscopic techniques operated at the synchrotron light sources. The use of apodized illumination in SXFM can be extended to the biologically important specimens. Apodized-illumination CDI of non-isolated objects can be usefully applied to various samples of material and biological importance with synchrotron X-rays (Miao *et al.*, 2003; Nishino *et al.*, 2009) and X-ray free-electron lasers (Seibert *et al.*, 2011; Kimura *et al.*, 2014).

Acknowledgements

This study was supported by CREST (JST); KAKENHI (JSPS) Grant Numbers 15H05737, 26870006, 26286077 and 23226004; the X-ray Free-Electron Laser Priority Strategy Program (MEXT); and the Cooperative Research Program of 'Network Joint Research Center for Materials and Devices'.

References

Fahrni, C. J. (2007). *Curr. Opin. Chem. Biol.* **11**, 121–127.
Fienup, J. R. (1982). *Appl. Opt.* **21**, 2758–2769.
Fittschen, U. E. A. & Falkenberg, G. (2011). *At. Spectrosc.* **66**, 567–580.
Gauderon, R., Lukins, P. B. & Sheppard, C. J. R. (1999). *Microsc. Res. Tech.* **47**, 210–214.

Ice, G. E., Budai, J. D. & Pang, J. W. L. (2011). *Science*, **334**, 1234–1239.
Jonge, M. D. de & Vogt, S. (2010). *Curr. Opin. Struct. Biol.* **20**, 606–614.
Khakurel, K. P., Kimura, T., Joti, Y., Matsuyama, S., Yamauchi, K. & Nishino, Y. (2015). *Opt. Express*, **23**, 28182–28190.
Kimura, T., Handa, S., Mimura, H., Yumoto, H., Yamakawa, D., Matsuyama, S., Inagaki, K., Sano, Y., Tamasaku, K., Nishino, Y., Yabashi, M., Ishikawa, T. & Yamauchi, K. (2009). *Jpn. J. Appl. Phys.* **48**, 072503.
Kimura, T., Joti, Y., Shibuya, A., Song, C., Kim, S., Tono, K., Yabashi, M., Tamakoshi, M., Moriya, T., Oshima, T., Ishikawa, T., Bessho, Y. & Nishino, Y. (2014). *Nat. Commun.* **5**, 3052.
Kimura, T., Matsuyama, S., Yamauchi, K. & Nishino, Y. (2013). *Opt. Express*, **21**, 9267–9276.
Kirkpatrick, P. & Baez, A. V. (1948). *J. Opt. Soc. Am.* **38**, 766–774.
Maiden, M., Rodenburg, J. M. & Humphry, M. J. (2010). *Opt. Lett.* **35**, 2585–2587.
Majumdar, S., Peralta-Videa, J. R., Castillo-Michel, H., Hong, J., Rico, C. M. & Gardea-Torresdey, J. L. (2012). *Anal. Chim. Acta*, **755**, 1–16.
Marchesini, S., He, H., Chapman, H. N., Hau-Riege, S. P., Noy, A., Howells, M. R., Weierstall, U. & Spence, J. C. H. (2003). *Phys. Rev. B*, **68**, 140101.
Marrison, J., Räty, L., Marriott, P. & O'Toole, P. (2013). *Sci. Rep.* **3**, 2369.
Matsuyama, S., Nakamori, H., Goto, T., Kimura, T., Khakurel, K. P., Kohmura, Y., Sano, Y., Yabashi, M., Ishikawa, T., Nishino, Y. & Yamauchi, K. (2016). *Sci. Rep.* **6**, 24801.
Matsuyama, S., Shimura, M., Fujii, M., Maeshima, K., Yumoto, H., Mimura, H., Sano, Y., Yabashi, M., Nishino, Y., Tamasaku, K., Ishizaka, Y., Ishikawa, T. & Yamauchi, K. (2010). *X-ray Spectrom.* **39**, 260–266.
Miao, J., Charalambous, P., Kirz, J. & Sayre, D. (1999). *Nature (London)*, **400**, 342–344.
Miao, J., Hodgson, K. O., Ishikawa, T., Larabell, C. A., LeGros, M. A. & Nishino, Y. (2003). *Proc. Natl Acad. Sci. USA*, **100**, 110–112.
Miao, J., Ishikawa, T., Robinson, I. K. & Murnane, M. M. (2015). *Science*, **348**, 530–535.
Miao, J., Sayre, D. & Chapman, H. N. (1998). *J. Opt. Soc. Am. A*, **15**, 1662–1669.
Nishino, Y., Takahashi, Y., Imamoto, N., Ishikawa, T. & Maeshima, K. (2009). *Phys. Rev. Lett.* **102**, 018101.
Robinson, I. & Harder, R. (2009). *Nat. Mater.* **8**, 291–298.
Rodenburg, J. M., Hurst, A. C., Cullis, A. G., Dobson, B. R., Pfeiffer, F., Bunk, O., David, C., Jefimovs, K. & Johnson, I. (2007). *Phys. Rev. Lett.* **98**, 034801.
Sakdinawat, A. & Attwood, D. (2010). *Nat. Photon.* **4**, 840–848.
Schroer, C. G., Boye, P., Feldkamp, J. M., Patommel, J., Schropp, A., Schwab, A., Stephan, S., Burghammer, M., Schöder, S. & Riekel, C. (2008). *Phys. Rev. Lett.* **101**, 090801.
Seibert, M. M., Ekeberg, T., Maia, F. R. N. C., Svenda, M., Andreasson, J., Jönsson, O., Odić, D., Iwan, B., Rocker, A., Westphal, D., Hantke, M., DePonte, D. P., Barty, A., Schulz, J., Gumprecht, L., Coppola, N., Aquila, A., Liang, M., White, T. A., Martin, A., Caleman, C., Stern, S., Abergel, C., Seltzer, V., Claverie, J. M., Bostedt, C., Bozek, J. D., Boutet, S., Miahnahri, A. A., Messerschmidt, M., Krzywinski, J., Williams, G., Hodgson, K. O., Bogan, M. J., Hampton, C. Y., Sierra, R. G., Starodub, D., Andersson, I., Bajt, S., Barthelmess, M., Spence, J. C. H., Fromme, P., Weierstall, U., Kirian, R., Hunter, M., Doak, R. B., Marchesini, S., Hau-Riege, S. P., Frank, M., Shoeman, R. L., Lomb, L., Epp, S. W., Hartmann, R., Rolles, D., Rudenko, A., Schmidt, C., Foucar, L., Kimmel, N., Holl, P., Rudek, B., Erk, B., Hömke, A., Reich, C., Pietschner, D., Weidenspointner, G., Strüder, L., Hauser, G., Gorke, H., Ullrich, J., Schlichting, I., Herrmann, S., Schaller, G., Schopper, F., Soltau, H., Kühnel, K. U., Andritschke, R., Schröter, C. D., Krasniqi, F., Bott, M., Schorb, S., Rupp, D., Adolph, M., Gorkhover, T., Hirsemann, H., Potdevin, G., Graafsma, H., Nilsson, B., Chapman, H. N. & Hajdu, J. (2011). *Nature (London)*, **470**, 78–81.
Shapiro, D. A., Yu, Y. S., Tyliszczak, T., Cabana, J., Celestre, R., Chao, W., Kaznatcheev, K., Kilcoyne, A. L. D., Maia, F., Marchesini, S., Meng, Y. S., Warwick, T., Yang, L. L. & Padmore, H. A. (2014). *Nat. Photon.* **8**, 765–769.
Suzuki, Y., Takeuchi, A., Takano, H. & Takenaka, H. (2005). *Jpn. J. Appl. Phys.* **44**, 1994–1998.
Takahashi, Y., Nishino, Y., Tsutsumi, R., Kubo, H., Furukawa, H., Mimura, H., Matsuyama, S., Zettsu, N., Matsubara, E., Ishikawa, T. & Yamauchi, K. (2009). *Phys. Rev. B*, **80**, 054103.
Tamasaku, K., Tanaka, Y., Yabashi, M., Yamazaki, H., Kawamura, N., Suzuki, M. & Ishikawa, T. (2001). *Nucl. Instrum. Methods Phys. Res. A*, **467–468**, 686–689.
Thibault, P., Dierolf, M., Menzel, A., Bunk, O., David, C. & Pfeiffer, F. (2008). *Science*, **321**, 379–382.
Thibault, P. & Menzel, A. (2013). *Nature (London)*, **494**, 68–71.
Webb, R. H. (1996). *Rep. Prog. Phys.* **59**, 427–471.